Spatio-temporal characteristics of the equatorial ionization anomaly (EIA) in the East African sector using ionospheric tomography

Tsegaye Kassa Gogie

Washera Geospace and Radar Science Laboratory, Department of Physics, College of Science, Bahir Dar University, E-mail:-tsegaye8684@gmail.com

Advisors: B. Damtie (BDU, Ethiopia), P. Cilliers (SANSA) and E. Yizengaw (USA)

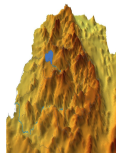**Venue:** Kyushu University, Fukuoka, Japan

Outline

A glance on Bahir Dar University!

Project overview

Ionospheric research is **still active**

Researchers are working on **theoretical** and **empirical** models, which are assisted by different measurements

This effort results in **global image of the ionosphere**

However, **in order to capture the spatial** and **temporal** characteristics of the ionosphere **regional** theoretical and empirical investigations are vey important

Ionospheric research

Model-based   Experiment-based
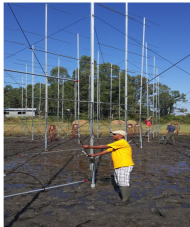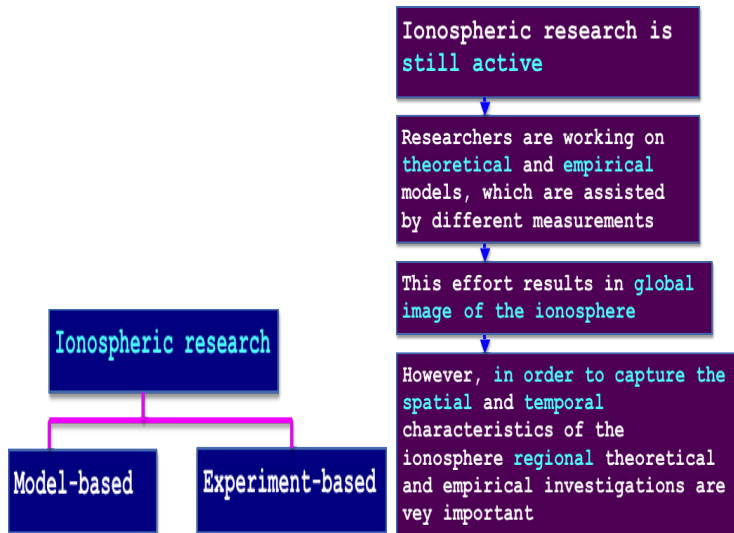
Cont···

Theoretical

Solve **conservation equations numerically** as a function of space and time

Require magnetospheric and atmospheric **inputs**

Outputs: Calculate plasma density, temperature and flow velocity

Are powerful to understand the **physical** and **chemical** processes of the upper atmosphere

Example: The Sheffield Coupled Thermosphere Ionosphere Plasmasphere Model (**CTIP**)

Cont···

Empirical

Analytical descriptions of the ionosphere with functions derived from **experimental data** or **adopted from physical models**

The two known empirical models are **International reference ionosphere** (IRI) and **NeQuick**

IRI

Its data sources include
- Coefficients such as **foF2** from ground-based sounders
- Incoherent scatter measurements
- Topside sounder ionograms
- In-situ measurements

Cont···

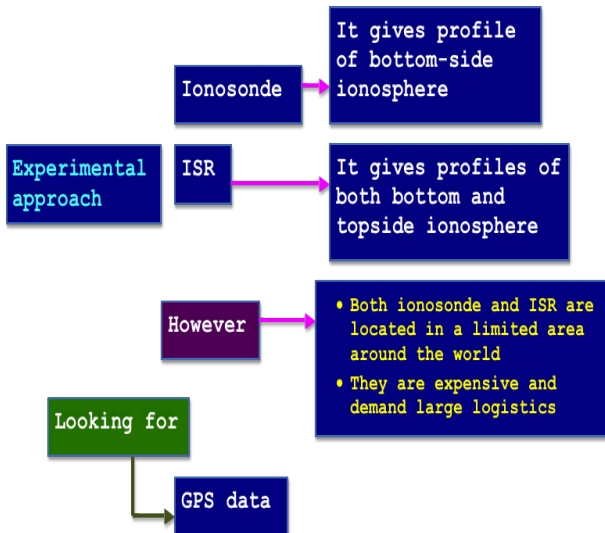**Inputs**

- Location
- Time
- Date

In the altitude range of 50-2000 km

Outputs

- Electron temperature
- Ion temperature
- Total electron content (TEC)

Cont···

Ionosonde → It gives profile of bottom-side ionosphere

Experimental approach

ISR → It gives profiles of both bottom and topside ionosphere

However →
- Both ionosonde and ISR are located in a limited area around the world
- They are expensive and demand large logistics

Looking for

GPS data

Cont···

GPS data

Can measure TEC

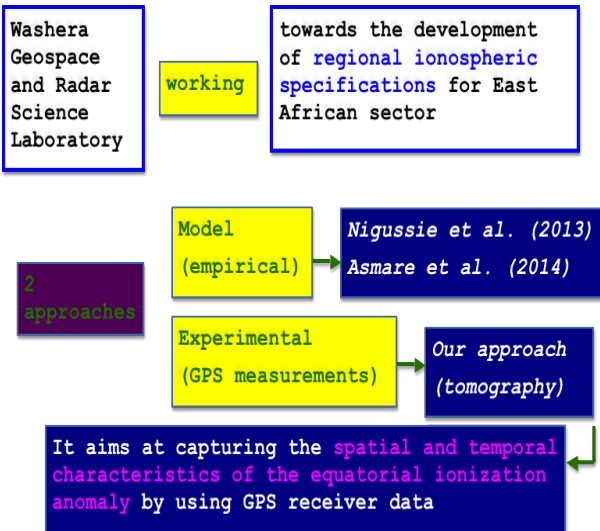Installing various GPS receivers around the world can make this measurement

It is possible to create a global view of the ionosphere by utilizing all possible data merging them together and interpolating them

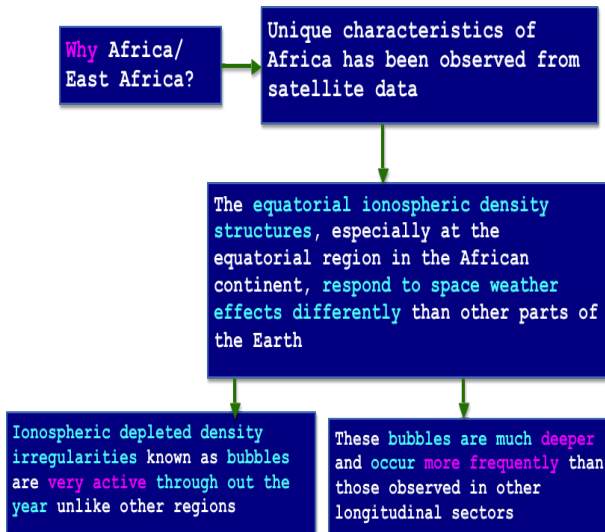The TEC can be inverted to estimate the electron density at different height (Ionospheric tomography)

Cont···

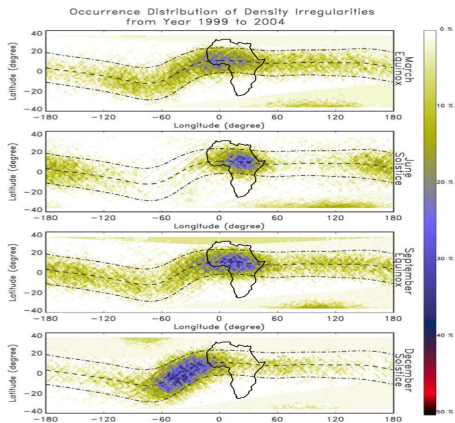Washera Geospace and Radar Science Laboratory

working

towards the development of regional ionospheric specifications for East African sector

2 approaches

Model (empirical)

Nigussie et al. (2013)
Asmare et al. (2014)

Experimental (GPS measurements)

Our approach (tomography)

It aims at capturing the spatial and temporal characteristics of the equatorial ionization anomaly by using GPS receiver data

Cont···

Why Africa/ East Africa?

→ Unique characteristics of Africa has been observed from satellite data

↓

The equatorial ionospheric density structures, especially at the equatorial region in the African continent, respond to space weather effects differently than other parts of the Earth

↓

Ionospheric depleted density irregularities known as bubbles are very active through out the year unlike other regions

These bubbles are much deeper and occur more frequently than those observed in other longitudinal sectors
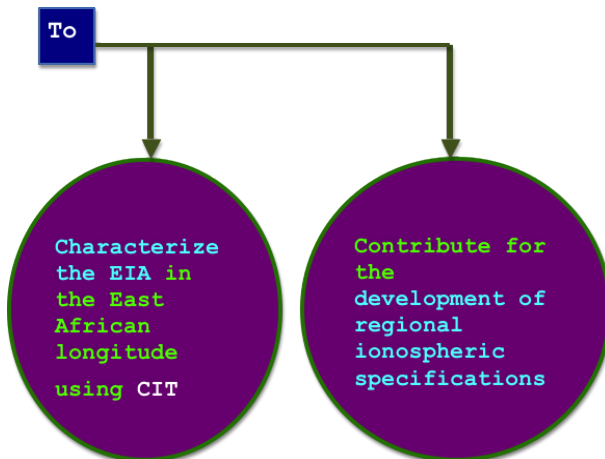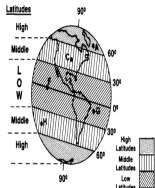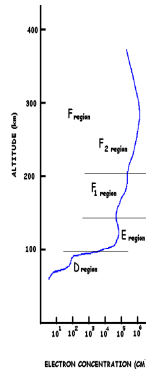
Cont···

Figure: Distribution of irregularities from year 1999-2004 over Africa (*Groves et al., 2012*).

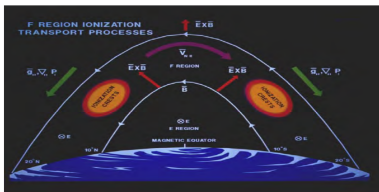## Objectives

To

Characterize the EIA in the East African longitude using **CIT**

Contribute for the development of regional ionospheric specifications

Ionospheric regions

Ionospher → Vertical, Latitudinal

Vertical → D, E, F

D: Formed by hard X-ray and Lyman alpha radiation

E:
- normal region
- auroral region
- Sporadic layer

F:
- has greatest electron density
- the most variable
- composed mostly of atomic oxygen

Latitudinal → High, Mid, Low

High:
- characterized by particle precipitation and longitudinally distributed electron density depletion

Mid:
- Motion of plasma due to neutral wind and electric field and follows magnetic field lines
- The plasma tends to co-rotate with the earth
- Electron density gradients tend to be weaker than those of the Equatorial latitude.

Low:
- EEJ
- Spread F
- EIA

Latitudes
- High 90°
- Middle 60°
- LOW 30° 0°
- Middle 60°
- High 90°

High Latitudes / Middle Latitudes / Low Latitudes

F_{region}
F_2 region
F_1 region
E_{region}
D_{region}

ALTITUDE (km)

ELECTRON CONCENTRATION (CM⁻³)

Formation and dynamics of the EIA
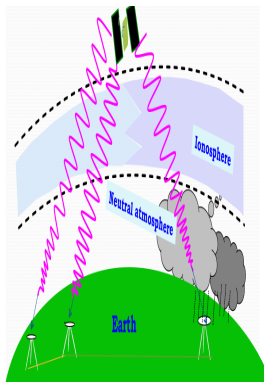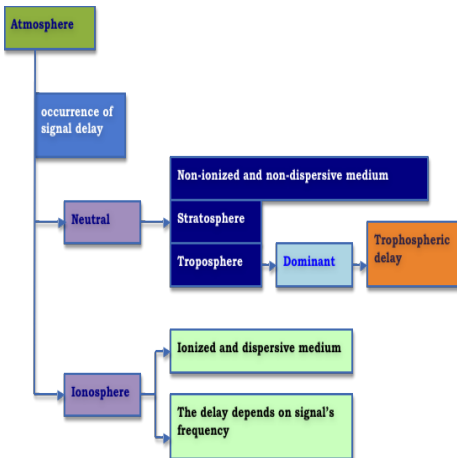
Data

Data of the year 2012

GPS signal and atmospheric effects

Each satellite transmits two carrier electromagnetic waves with frequencies, both in the L-band

L1 = 1575.42 MHz,   λ1 = 19 cm
L2 = 1227.60 MHz,   λ2 = 24 cm

Atmosphere

occurrence of signal delay

Neutral

- Non-ionized and non-dispersive medium
- Stratosphere
- Troposphere → Dominant → Trophospheric delay

Ionosphere

- Ionized and dispersive medium
- The delay depends on signal's frequency

Ionospheric delay

- When passing through the atmosphere, the electromagnetic signals experience changes in velocity (speed and direction) due to the refraction.

- According to Fermat's principle, the measured range l is given by the integral of the refractive index n along the ray path from the satellite to receiver:

$$l = \int_{rp} n\,dl. \tag{1}$$

- Accordingly, the signal's delay can be written as

$$\Delta = \int_{rp} n\,dl - \int_{sl} dl, \tag{2}$$

where the second integral is the Euclidean distance between the satellite and receiver.

- Eq. (2) includes both the signal bending and propagation delay.

- One of the possible simplification can be obtained by approximating the first integral along the straight line between the satellite and receiver:

$$\Delta = \int_{sl} (n - 1)\,dl. \tag{3}$$

Dual frequency GPS signal in extracting ionospheric TEC

- A medium where the wave propagation speed and hence the refractive index depend on the frequency or the angular frequency ω and the wave number k are not proportional is a dispersive medium.
- This is also valid for the ionosphere where ω and k are related, to a first approximation

$$\omega^2 = c^2 k^2 + \omega_p^2, \tag{4}$$

where c is the propagation speed of a signal in a vacuum and $\omega_p = 2\pi f_p$, where $f_p = 8.98\sqrt{N_e}$ in Hz and N_e is the electron density (in $\frac{e}{m^3}$). Eq. (4) is called the relation of dispersion of the ionosphere, and ω_p is called the critical frequency of the ionospheric plasma.

Four GPS range measurements

$$P_1 = \rho +_{\triangle_{gr,1}} + \tau_1^r + \tau_1^s$$

$$P_2 = \rho +_{\triangle_{gr,2}} + \tau_2^r + \tau_2^s$$

$$L_1 = \rho +_{\triangle_{ph,1}} + N_1\lambda_1 + \varepsilon_1^r + \varepsilon_1^s$$

$$L_2 = \rho +_{\triangle_{ph,2}} + N_2\lambda_2 + \varepsilon_2^r + \varepsilon_2^s$$

where P_i = measured code ranges

L_i = measured phase ranges (i = 1, 2) on the

L_1 and L_2 frequencies

$\triangle_{gr,i}$ = group ionospheric delay term

$\triangle_{ph,i}$ = phase ionospheric delay term

λ_i = carrier wavelength

N_i = int eger cycle ambiguity

τ_i, ε_i = dispersion components of

the satellite and the reciever hardware delays

Usefull relations

$$n_{ph} = 1 - \frac{40.3}{f^2} Ne$$

$$n_{gr} = 1 + \frac{40.3}{f^2} Ne$$

$$\triangle_{ph,f} = -\frac{40.3}{f^2} \int Ne\, dl = -\frac{40.3}{f^2} I$$

$$\triangle_{gr,f} = \frac{40.3}{f^2} \int Ne\, dl = \frac{40.3}{f^2} I, \text{where } I = sTEC = \int Ne\, dl$$

Cont$\cdots$

- If we neglect terms other than ρ, $\Delta_{ph,i}$ and $\Delta_{gr,i}$ we may have

$$
\begin{align}
P_1 &= \rho + \Delta_{gr,1} \tag{5} \\
P_2 &= \rho + \Delta_{gr,2} \tag{6} \\
L_1 &= \rho + \Delta_{ph,1} \tag{7} \\
L_2 &= \rho + \Delta_{ph,2}. \tag{8}
\end{align}
$$

- The dual frequency differencing of the code and phase ranges gives the ionospheric combinations P_I and L_I:

$$
P_I = P_2 - P_1 \quad = \quad \rho + \Delta_{gr,2} - (\rho + \Delta_{gr,1}) = \rho + \frac{f_1^2}{f_2^2}\Delta_{gr,1} - \rho - \Delta_{gr,1} \tag{9}
$$

$$
L_I = L_1 - L_2 \quad = \quad \rho + \Delta_{ph,1} - (\rho + \Delta_{ph,2}) = \rho + \Delta_{ph,1} - \rho - \frac{f_1^2}{f_2^2}\Delta_{ph,1}. \tag{10}
$$

- Thus we have

$$
P_I = P_2 - P_1 \quad = \quad \frac{f_1^2}{f_2^2}\Delta_{gr,1} - \Delta_{gr,1} = \Delta_{gr,1}\left(\frac{f_1^2}{f_2^2} - 1\right) \tag{11}
$$

$$
L_I = L_1 - L_2 \quad = \quad \Delta_{ph,1} - \frac{f_1^2}{f_2^2}\Delta_{ph,1} = \Delta_{ph,1}\left(1 - \frac{f_1^2}{f_2^2}\right).
$$

Cont···

- By using the relations $\Delta_{ph,1} = -\frac{40.3}{f_1^2} sTEC_P$ and $\Delta_{gr,1} = \frac{40.3}{f_1^2} sTEC_L$ we get

$$P_2 - P_1 = \frac{40.3}{f_1^2} sTEC \left(\frac{f_1^2}{f_2^2} - 1 \right) = 40.3 \left(\frac{f_1^2 - f_2^2}{f_1^2 f_2^2} \right) sTEC_P \tag{13}$$

$$L_1 - L_2 = -\frac{40.3}{f_1^2} sTEC \left(1 - \frac{f_1^2}{f_2^2} \right) = -40.3 \left(\frac{f_2^2 - f_1^2}{f_1^2 f_2^2} \right) sTEC_L. \tag{14}$$

- From Eqs. (13) and (14) we get

$$sTEC_P = \frac{1}{40.3} \left(\frac{f_1^2 f_2^2}{f_1^2 - f_2^2} \right) (P_2 - P_1) \tag{15}$$

$$sTEC_L = \frac{1}{40.3} \left(\frac{f_1^2 f_2^2}{f_1^2 - f_2^2} \right) (L_1 - L_2), \tag{16}$$

where $sTEC_P$ is the slant total election content from code measurements and $sTEC_L$ is the slant total election content from phase measurements.

- If we consider the differencing of the code and the phase ranges including the biases and other terms we get

$$P_I = P_2 - P_1 = 40.3 \left(\frac{1}{f_2^2} - \frac{1}{f_1^2} \right) sTEC_P + B_r + B_s \tag{17}$$

$$L_I = L_1 - L_2 = 40.3 \left(\frac{1}{f_2^2} - \frac{1}{f_1^2} \right) sTEC_L + (N_1\lambda_1 - N_2\lambda_2) + B_r' + B_s' \tag{18}$$

Cont···

- The code range ionospheric combination P_I is absolute, but noisy.

- On the other hand, the phase combination, L_I, is smooth and can provide very accurate measurements of TEC changes, but is offset from the code range combination by a bias related to the unknown integer cycle ambiguity, $N_1 \lambda_1 - N_2 \lambda_2$.

- The ambiguity (phase leveling) is removed by averaging ($sTEC_P - sTEC_L$) over a satellite pass (phase connecting arc) as

$$sTEC_{leveled} = sTEC_L - mean(sTEC_L - sTEC_P)$$

(19)

- This "levels" the TEC to the unambiguous.

Methods of analysis
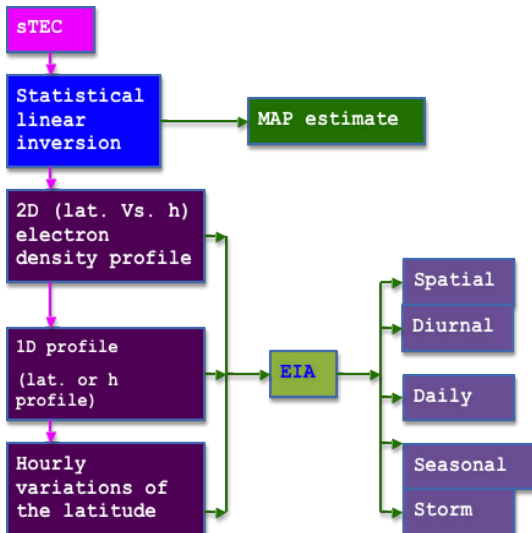
Formulating statistical linear inverse problem

- The sTEC and the ionospheric electron density (Ne) can be related by

$$\mathbf{sTEC} = \int_{l} Ne(\phi, \lambda, h, t) ds, \tag{20}$$

  where ϕ, λ, h and t stand for latitude, longitude, altitude and time variables respectively and l refers the ray propagation path of each GPS satellite-receiver pair.

- For 2D case, the sTEC can be formulated as

$$\mathbf{sTEC} = \int_{l} Ne(\phi, h) ds. \tag{21}$$

- The discretized version of Eq. (21) becomes

$$\mathbf{sTEC_i} = \sum_{j=1}^{n} A_{ij} Ne_j + \varepsilon_i, \tag{22}$$

  where i is the ith measurement along propagation path of each GPS satellite-receiver pair.

Cont···

- Eq. (22) can be generally written in simple matrix notation as:

$$y_{m \times 1} = A_{m \times n} x_{n \times 1} + \varepsilon_{m \times 1}, \tag{23}$$

  where n is the number of pixels in the image, m is the number of $sTEC$ measurements, y is a column vector of the m known $sTEC$ measurements, A is an $m \times n$ projection matrix with A_{ij} being the length of ray i traversing pixel j, x is a column vector consisting of all the unknown electron densities (Ne) in all the pixels, and ε is a column vector associated with additive measurement noises.

- Let the electron density vector, x and the measurement error vector, ε be independent, jointly distributed random variables with $x \sim \mathrm{Normal}(\mu_n, \Sigma_r)$ and $\varepsilon \sim \mathrm{Normal}(0_m, \Sigma_\varepsilon)$ where μ_n, Σ_r, 0_m and Σ_ε are mean of the unknown, covariance of the unknown, mean and covariance of the measurement error respectively.

- If A be an $m \times n$ matrix, we can define a new random vector

$$y = Ax + \varepsilon. \tag{24}$$

Cont···

Solving statistical linear inverse problem in Bayesian framework

- If the measurement errors are Gaussian with zero mean, the a posteriori probability density of the unknown, x, according to Bayesian framework, given its priori density, $\pi_{\mathrm{pr}}(\mathbf{x})$, and measurement vector, y, can be spelled out as

$$\pi_{\mathrm{post}}(\mathbf{x}) = \pi(\mathbf{x}|\mathbf{y}) = \frac{\pi_{\mathrm{pr}}(\mathbf{x}) \times \pi(\mathbf{y}|\mathbf{x})}{\pi(\mathbf{y})}, \tag{25}$$

where $\pi_{\mathrm{pr}}(\mathbf{x})$ is the joint a priori density of the unknowns and the marginal density $\pi(\mathbf{y}) = \int_{\mathbb{R}^m} \pi(\mathbf{x}, \mathbf{y}) d\mathbf{x} = \int_{\mathbb{R}^m} \pi(\mathbf{y}|\mathbf{x}) \pi_{\mathrm{pr}}(\mathbf{x}) d\mathbf{x}$ is can be seen as a norming constant and usually of little importance.

- The expression $\pi(\mathbf{y}|\mathbf{x}) \propto \exp\left[-\frac{1}{2}(\mathbf{y} - \mathbf{Ax})^{\mathrm{T}} \Sigma_{\varepsilon}^{-1}(\mathbf{y} - \mathbf{Ax})\right]$ is called the likelihood function, as it expresses the likelihood of different measurement outcomes when $\mathbf{x} = \mathbf{x}$ is given.
  ### Maximum Likelihood Estimate (MLE)

- If we don't consider a prior information, $\pi_{\mathrm{pr}}(\mathbf{x})$ can be constant and thus the most probable values of the unknown can be computed by maximizing $\pi(\mathbf{x}|\mathbf{y}) = \pi(\mathbf{y}|\mathbf{x}) \propto \exp\left[-\frac{1}{2}(\mathbf{y} - \mathbf{Ax})^{\mathrm{T}} \Sigma_{\varepsilon}^{-1}(\mathbf{y} - \mathbf{Ax})\right]$ with respect to the unknown x. That means differentiating the above expression with respect to x and letting to be zero.

$$-\left(\frac{d}{d\mathbf{x}}(\mathbf{Ax})\right)^{\mathbf{T}} \Sigma_{\varepsilon}^{-1}(\mathbf{y} - \mathbf{Ax}) - (\mathbf{y} - \mathbf{Ax})^{\mathbf{T}} \Sigma_{\varepsilon}^{-1} \frac{d}{d\mathbf{x}}(\mathbf{Ax}) = 0. \tag{26}$$

Since Σ_{ε} is symmetric ($\Sigma_{\varepsilon} = \Sigma_{\varepsilon}^{\mathbf{T}}$) and nonsingular then $\Sigma_{\varepsilon}^{-1}$ is also symmetric ($\Sigma_{\varepsilon}^{-1} = (\Sigma_{\varepsilon}^{-1})^{\mathbf{T}}$).

Cont···

- This implies that the matrix multiplication, $A^T \Sigma_\varepsilon^{-1} B = B^T \Sigma_\varepsilon^{-1} A$, is valid.

- Applying the above matrix multiplication identity into Eq. (26) gives

$$- \left(\frac{d}{d\mathbf{x}} (\mathbf{Ax}) \right)^T \Sigma_\varepsilon^{-1} (\mathbf{y} - \mathbf{Ax}) - \left(\frac{d}{d\mathbf{x}} (\mathbf{Ax}) \right)^T \Sigma_\varepsilon^{-1} (\mathbf{y} - A\mathbf{x}) = 0. \tag{27}$$

- This in turn yields

$$- 2 \left(\frac{d}{d\mathbf{x}} (\mathbf{Ax}) \right)^T \Sigma_\varepsilon^{-1} (\mathbf{y} - \mathbf{Ax}) = 0. \tag{28}$$

- Differentiation and further mathematical manipulations simplify the above equation into

$$\mathbf{A}^T \Sigma_\varepsilon^{-1} (\mathbf{y} - \mathbf{Ax}) = 0$$

$$\mathbf{A}^T \Sigma_\varepsilon^{-1} \mathbf{y} = \mathbf{A}^T \Sigma_\varepsilon^{-1} \mathbf{Ax}. \tag{29}$$

- The resulting solution, which is known as the Maximum Likelihood Estimate (MLE), is given by

$$\boxed{\mathbf{x}_{\mathrm{MLE}} = (\mathbf{A}^T \Sigma_\varepsilon^{-1} \mathbf{A})^{-1} \mathbf{A}^T \Sigma_\varepsilon^{-1} \mathbf{y}.}$$
(30)

Maximum A Posteriori (MAP) Estimate

- An obvious limitation occurs on the maximum likelihood estimate of Eq. (30) when the inverse matrix $(\mathbf{A}^{\mathrm{T}}\Sigma_\varepsilon^{-1}\mathbf{A})^{-1}$ do not exist.

- However, even when the inverse matrix exists, it can still be ill-conditioned (become nearly singular).

- In this case our solution would be extremely unstable and unrealistic.

- The instability of Eq. (30) exhibit too strong point-to-point variations in the inversion.

- To overcome this problem, we need to find a way of limiting these variations (we have to apply regularization methods).

- To do so, let us consider two neighboring grid points (pixels) p_i and p_j located at the same altitude or at the same latitude. If we assume that the difference of electron densities at these points is close to zero, we incorporate some error ε_r^{ij}.

- This can be formulated as

$$0 = \mathrm{x}_i - \mathrm{x}_j + \varepsilon_r^{ij}. \tag{31}$$

- If we do this for all vertical and horizontal differences of neighboring grid points, the resulting system of equations can be expressed in a single matrix form as

$$0 = \mathbf{A}_{\mathrm{r}}\mathbf{x} + \varepsilon_{\mathrm{r}}, \tag{32}$$

where $\mathbf{A}_{\mathrm{r}}$ is regularization matrix with elements $+1, -1$ and 0 in appropriate places. We can now combine Eq. (24) and (32) to get a single matrix equation as

$$\left(\begin{array}{c} \mathbf{y} \\ \mathbf{0} \end{array} \right) = \left(\begin{array}{c} \mathbf{A} \\ \mathbf{A_r} \end{array} \right) \mathbf{x} + \left(\begin{array}{c} \varepsilon \\ \varepsilon_{\mathbf{r}} \end{array} \right). \tag{33}$$

Cont···

- The regularized a posterior density, $\pi_{\mathrm{post}}(\mathbf{x}) = \pi(\mathbf{x}|\mathbf{y}, \mathbf{0})$, can be written as

$$\pi_{\mathrm{post}}(\mathbf{x}) = \pi(\mathbf{x}|\mathbf{y}, \mathbf{0}) \quad \propto \quad \exp\left[-\frac{1}{2}(\mathbf{A_r x})^{\mathrm{T}}\Sigma_{\mathbf{r}}^{-1}(\mathbf{A_r x})\right] \times \exp\left[-\frac{1}{2}(\mathbf{y}-\mathbf{Ax})^{\mathrm{T}}\Sigma_{\varepsilon}^{-1}(\mathbf{y}-\mathbf{Ax})\right],$$

where $\pi_{\mathrm{pr}}(\mathbf{x}) \propto \exp\left[-\frac{1}{2}(\mathbf{A_r x})^{\mathrm{T}}\Sigma_{\mathbf{r}}^{-1}(\mathbf{A_r x})\right]$ is the distribution of difference prior with covariance matrix $\Sigma_{\mathbf{r}}$.

- By applying a similar maximization for the posteriori distribution given by Eq. (34), we can compute the most probable values of the unknowns as

$$\left(\frac{d}{d\mathbf{x}}(\mathbf{A_r x})\right)^{\boldsymbol{T}}\Sigma_{\mathbf{r}}^{-1}(\mathbf{A_r x}) - \left(\frac{d}{d\mathbf{x}}(\mathbf{Ax})\right)^{\boldsymbol{T}}\Sigma_{\varepsilon}^{-1}(\mathbf{y}-\mathbf{Ax}) - (\mathbf{y}-\mathbf{Ax})^{\boldsymbol{T}}\Sigma_{\varepsilon}^{-1}\frac{d}{d\mathbf{x}}(\mathbf{Ax}) = 0. \tag{34}$$

- Handling the differentiation with respect to x and applying the matrix multiplication identity, $A^{\boldsymbol{T}}\Sigma_{\varepsilon}^{-1}B = B^{\boldsymbol{T}}C_{\varepsilon}^{-1}A$, will lead us to have

$$2\mathbf{A_r}^{\boldsymbol{T}}\Sigma_{\mathbf{r}}^{-1}\mathbf{A_r x} - 2\mathbf{A}^{\boldsymbol{T}}\Sigma_{\varepsilon}^{-1}\mathbf{y} + 2\mathbf{A}^{\boldsymbol{T}}\Sigma_{\varepsilon}^{-1}\mathbf{Ax} = 0. \tag{35}$$

- Further rearrangements result in

$$(\mathbf{A_r}^{\boldsymbol{T}}\Sigma_{\mathbf{r}}^{-1}\mathbf{A_r} + \mathbf{A}^{\boldsymbol{T}}\Sigma_{\varepsilon}^{-1}\mathbf{A})\mathbf{x} - \mathbf{A}^{\boldsymbol{T}}\Sigma_{\varepsilon}^{-1}\mathbf{y} = 0. \tag{36}$$

- Solving for $\mathbf{x} = \mathbf{x}_{\mathrm{MAP}}$ gives

$$\boxed{\mathbf{x}_{\mathrm{MAP}} = (\mathbf{A}^{\mathrm{T}}\Sigma_{\varepsilon}^{-1}\mathbf{A} + \mathbf{A_r}^{\mathrm{T}}\Sigma_{\mathbf{r}}^{-1}\mathbf{A_r})^{-1}\mathbf{A}^{\mathrm{T}}\Sigma_{\varepsilon}^{-1}\mathbf{y}.} \tag{37}$$

- Eq. (37) is commonly known as Maximum of a Posteriori Estimate (MAP) of the unknowns.

Cont···

- We have used Chapman profile as a priori profile of the Ne in the form of priori covariance matrix, Σ_r.

- The variance (error) estimate of the statistical linear inversion can be obtained from the posterior covariance matrix, $\mathbf{pcovmat} = (\mathbf{A}^T \Sigma_\varepsilon^{-1} \mathbf{A} + \mathbf{A}_r^T \Sigma_r^{-1} \mathbf{A}_r)^{-1}$, in such a way that the diagonal elements of this matrix belong to the square of the variances of the estimated error.

- Thus the variances, which are the square root of the diagonal elements of the posterior covariance matrix, can be considered as the error estimate of the employed inversion approach.

Sample ray path and the EIA movement/dimension from vTEC
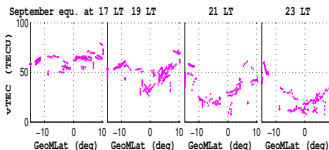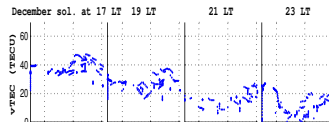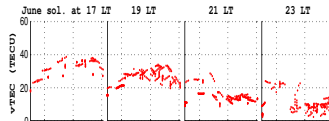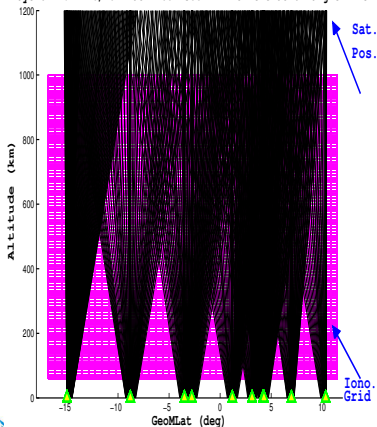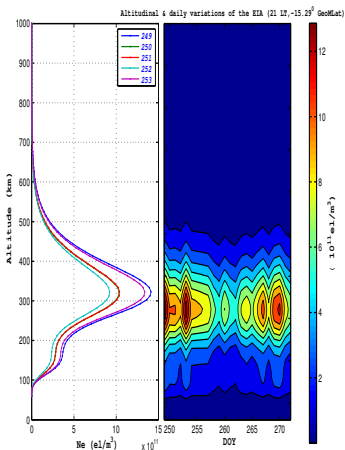
Validation
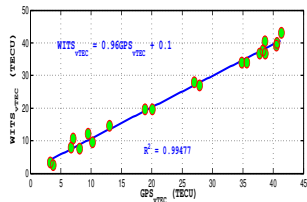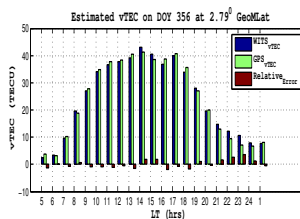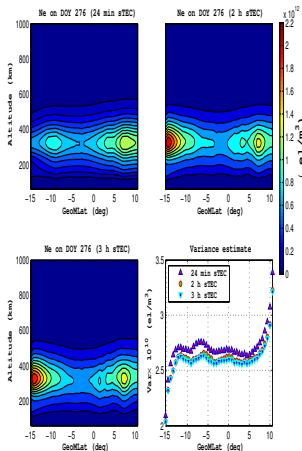
Diurnal and seasonal variations of the EIA
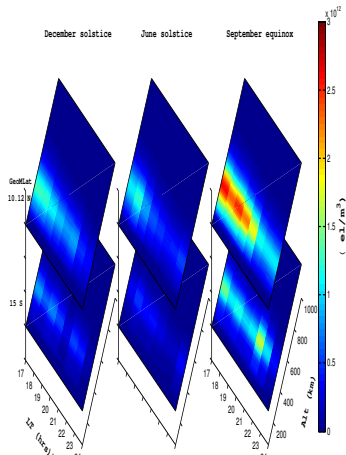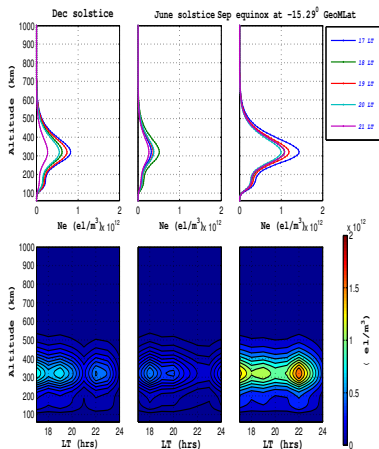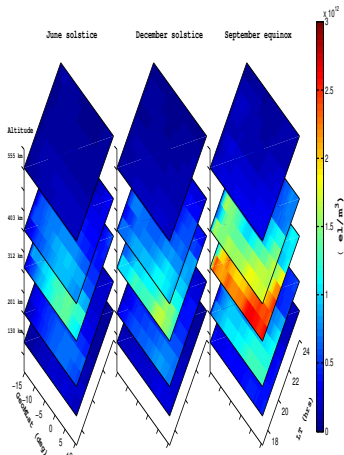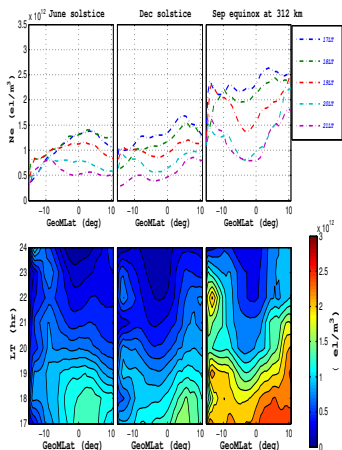
Cont···

Cont···
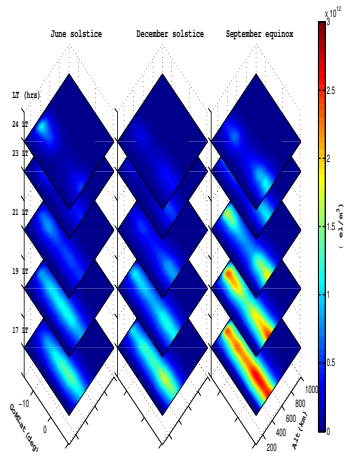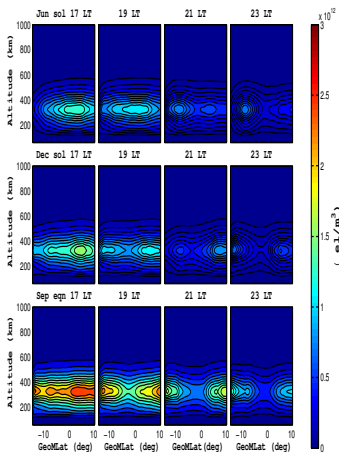
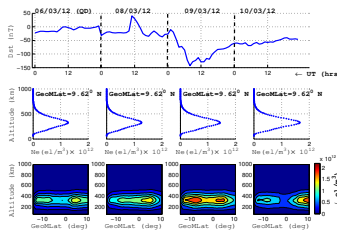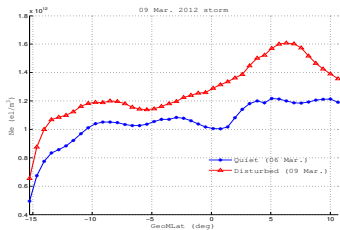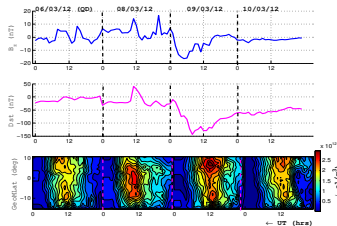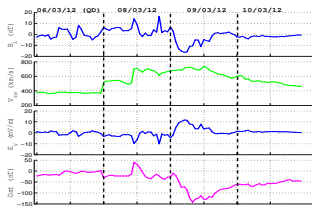# Daily variations of the EIA
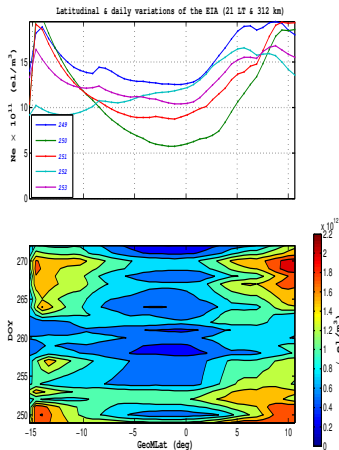
Cont···
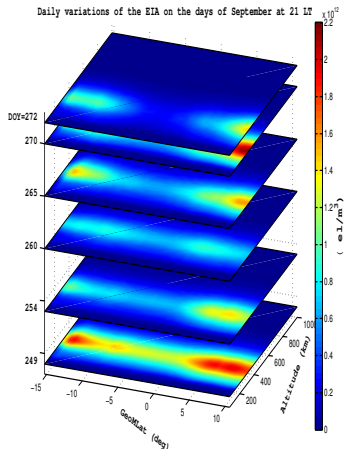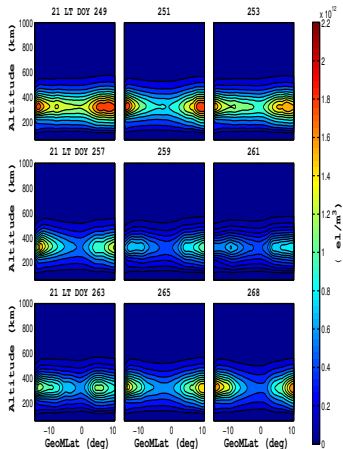
Storm-time responses: 09 March 2012 storm

Temporal variations of NmF2 of the EIA
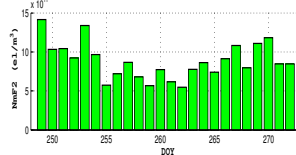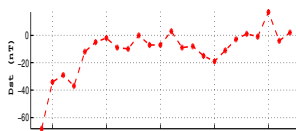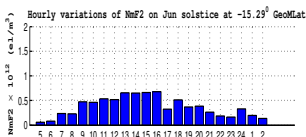
Spatial variations of the EIA

- The spatial variations of the EIA can be seen in terms of its altitude and latitude profile of the EIA at 21:00 LT in a particular day (DOY 356) and season (December solstice).

- This can be seen from the middle panel of Fig. (35) at 21:00 LT. In this Fig., it is manifested that the maximum of the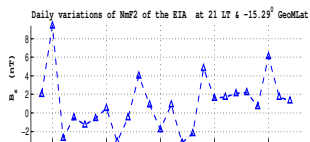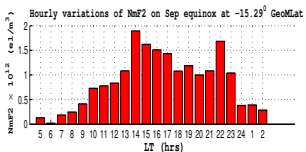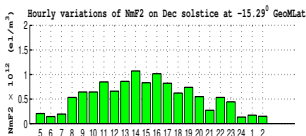 EIA is appeared around 312 km and its thickness along the altitude is found to be between 180 km to 450 km (270 km) during December solstice.

- Moreover, the latitude profile of the EIA advocated that the ionosphere is pinched around the equator and thickened around 6.3^0 N to 11^0 N GeoMLat (with a thickness of $5^0 \simeq 555$ km).

- This might be explained by an ionization transport mechanism commonly referred to as the equatorial fountain effect and the later downward diffusion of ionization along the magnetic field lines (Andreeva et al., 2000).

Conclusions

- We have produced the images of the EIA by applying Bayesian inversion theory.
- We have described the temporal, spatial and storm-time variations of the EIA. The diurnal variations of EIA was found to be dependent on the position of the sun over the horizon and the daily variations have been explained by the occurrence of storm events.
- We have also shown that the EIA behaves differently on different seasons and pronounced EIA has been observed during Equinox than solstice seasons.
- Even if a sharp rise in EIA from about 09:00 to 16:00 LT was observed at all seasons, the strength is high in equinoctial months followed by December and June solstices.
- Seasonal variations of the EIA depend not only on production and loss of ionization but also on the transport of plasma through winds and on thermospheric neutral composition variations.
- The strong EIA in equinox months are due to high values of solar intensity.
- Due to the combined effect of the trans-equatorial wind and the auroral equator-ward wind there is an occurrence of an asymmetry of the two crests of the EIA.

Cont···

- During solstice the two crests move equator ward but during equinox the two crests move slightly poleward.
- The investigation on the spatial parameters has shown that the EIA varies along both altitude and latitude coordinates.
- The synthesis on the peak of the EIA (NmF2) has demonstrated a significant dependence of NmF2 on local time, day and season of the year.
- The storm-time analysis has also reveled that the EIA responds differently during geomagnetically disturbed and stable situations.
- The enhanced EIA at 18:00 UT (longer time after the onset of the storm) might be observed by the disturbance dynamo electric field due to the storm-time circulation (*Fejer and Scherliess, 1995*).
- In terms of the the appearance of the daytime EIA (the peak and the width), we have observed that the northern crest predominately appeared well whereas the southern anomaly relatively inhibited during the geomagnetic storm we considered.
- This implies that the effect of the storm has a clear latitudinal (spatial) dependance or means that the effects of storm has propagated along the latitude.

1. **Kassa T.**, Damtie B., Bires A., Yizengaw E. & Cilliers P. **Storm-time characteristics of the equatorial ionization anomaly in the East African sector**. *Adv. Space Res.*, 04 February 2015, *The revised version of the article is submitted to the journal*.

2. Mengistu E. & **Kassa T.** **Temporal characteristics of Equatorial Electrojet and Counter Electrojet over Ethiopian sector**. *Adv. Space Res.*, October 2014, `http://dx.doi.org/10.1016/j.asr.2014.10.031`.

3. **Kassa T.**, Damtie B., Bires A., Yizengaw E. & Cilliers P. **Spatio-temporal characteristics of the Equatorial Ionization Anomaly (EIA) in the East African region via ionospheric tomography during the year 2012**. *Adv. Space Res.*, 55 (2015) 184-198, avilable online on September 2014, `http://dx.doi.org/10.1016/j.asr.2014.09.001`.

4. Asmare Y., **Kassa T.** & Nigussie M. **Validation of IRI-2012 TEC model over Ethiopia during solar minimum (2009) and solar maximum (2013) phases**. *Adv. Space Res.*, **53** (1), 1582-1594, February 2014, `http://dx.doi.org/10.1016/j.asr.2014.02.017`.

5. Chartier A., Kinrade J., Mitchell C., Rose J., Jackson D., Cilliers P., Habarulema J., Katamzi Z., Mckinnell L., Matamba T., Opperman B., Ssessanga N., Mezgebe S., Tyalimpi V., Franceschi G., Notarpietro R., Romano V., Scotto C., Dovis F., Avenant E., Wonnacott R., Oyeyemi E., Mahrous A., Mengistu G., Lekamisy H. , Olwendo J., Sibanda P., **Kassa T.** & Rabiu B. **Ionospheric Imaging in Africa**. *Radio Sci.*, **49**, doi: 10.1002/2013 RS005238, USA, January 2014.

6. **Kassa T.**, Damtie B. & Yizengaw E. **The Response of Ethiopian Ionosphere to the Magnetic Storm of 11 October 2008**. *LAJPE*, **6**, Mexico, June 2012.

7. **Kassa T.** & Damtie B., Hydrostatic Equilibrium in modeling the neutral atmosphere. *LAJPE*, **4** (2), Mexico, May 2010.

Accepted conference papers

1. **Kassa T.**, Damtie B., Bires A., Yizengaw E. & Cilliers P. **Spatio-temporal characteristics of the Equatorial Ionization Anomaly (EIA) in the East African region via ionospheric tomography during the year 2012**. United Nations/Japan Workshop on Space Weather "Science and Data Products from ISWI Instruments", Fukuoka, Japan, 2-6 March 2015.

2. Aara'L Y. and **Kassa T. Statistics of ionospheric amplitude scintillation and its correlation with phase scintillation over Bahir Dar using GPS SCINDA during solar maximum phase**. Emerging Researchers National Conference in Science, Technology, Engineering and Mathematics (STEM), February 19-21 2015, Washington DC, USA.

3. **Kassa T.**, Tessema F., Bires A. and Nigussie M. Ionospheric response to Annular solar eclipse of 15 January 2010 and 03 November 2013 in the Ethiopian zone, the 4th Gondar School of Science and Technology, January 2014, Gondar University, Ethiopia.

4. **Kassa T.** Space Science activities and facilities at Washera Geospace and Radar Science Laboratory, Bahir Dar, Ethiopia, the 4th Gondar School of Science and Technology, January 2014, Gondar University, Ethiopia.

5. **Kassa T.** Characterizing the Ethiopian Ionosphere via GPS Observables and 2D electron density profile, ISWI/SCOSTEP, 21 October to 01 November 2013, Nairobi, Kenya.

6. **Kassa T.** Space Science activities at Washera Geospace and Radar Science Laboratory, ISWI/SCOSTEP, 21 October to 01 November 2013, Nairobi, Kenya.

7. **Kassa T.** Characterizing Equatorial Ionization Anomaly in Ethiopian sector, Beacon Satellite symposium, Bath University, 08-12 July 2013, UK.

8. **Kassa T.** Effects of 07 April 2011 and 22 January 2012 geomagnetic storms on GPS ionospheric observables at Bahir Dar , the 1st Annual Science Conference (ASC) organized by Science College, BDU, 31 May-01 June 2013, Gondar University, Ethiopia.

9. **Kassa T.** Characterizing Equatorial Ionization Anomaly in Ethiopian sector, Ionospheric monitoring workshop, Hermanus, 24-25 January 2013, South Africa.

10. **Kassa T.** Seasonal Variations of the Equatorial Anomaly Inferred from ground-based GPS Receivers in the Ethiopian Sector via Tomographic Study, the 2nd Gondar School of Science Technology, December 2012, Gondar University, Ethiopia.

Acknowledgment

I would like to acknowledge

1. My principal advisor Dr. B. Damtie and co-advisors, Dr. E. Yizengaw and Dr. P. Cilliers for the opportunity to pursue this research project.
2. NOAA, NASA, and UNAVCO databases in accessing solar and magnetospheric condition indicators, neutral density profiles and GPS TEC data respectively.
3. Reviewers & editors within *Adv. Space Res.* journal who have contributed for the publications of our papers.
4. Bahir Dar University, Office of Research and Community Service, Science College, Physics Department, Bahir Dar, Ethiopia.
5. The American Air Force Office of Scientific Researches (AFOSR), USA, under the project **Understanding the unique characteristics of equatorial ionosphere** (FA8655-13-1-3052).
6. The University of Oulu, Sodankyla Geophysical Observatory, Finland for their help through CIMO exchange scholarship program.
7. United Nations Office for Outer Space Affairs, Vienna, Austria
8. Kyushu University, ICSWSE, Fukuoka, Japan